PREDICTION OF THE COMA DRAG FORCE ON ROSETTA

Carlos Bielsa[(1) (2)], **Michael Müller** [(1)], **and Guillem Huguet**[(1) (2)]

(1)ESA/ESOC Flight Dynamics, HSO-GFS
Robert-Bosch-Str. 5, 64293 Darmstadt, Germany
+49-6151-90-4253, Carlos.Bielsa@esa.int, Michael.Mueller@esa.int

(2)GMV
Isaac Newton 11, P.T.M., 28760 Tres Cantos (Madrid), Spain
+34-91-8072100, cbielsa@gmv.com

Abstract: *When Rosetta operates in the vicinity of its target comet 67P/Churyumov-Gerasimenko, the drag force due to the coma gas is expected to be in the same order of magnitude as the gravity due to the comet nucleus. Hence the SC trajectory can only be predicted if the drag force on the SC can be predicted. The prediction of the drag force will be done empirically by scaling past measurements of the drag force to changed geometric conditions. The present paper aims at identifying methods that may be used to predict the drag force by incorporation of different available observables. The quality of each method is assessed by simulation in physically realistic coma. This is done under several idealistic assumptions of which the most important ones are: no time dependence of the coma, no gas compostion or dust-to-gas ratio variation, a constant nucleus surface temperature and no errors in measurement of coma observables. For the considered example cases (fly-bys at 5 and 10 km distance from the comet) the best methods, which incorporate measurements from remote-sensing instruments, reach an accuracy of 10-20% of the dV due to drag. The availability of reliable predictions of the drag force will ultimately depend on the fulfillment of these idealistic assumptions, particularly that of a time-independent coma.*

Keywords: *Rosetta, coma, comet, drag, atmosphere*

1. Introduction

The Rosetta spacecraft (SC) was launched in 2004 and will reach its target comet 67P/Churyumov-Gerasimenko (CG) in 2014. Currently in hibernation, it will not be reactivated until January 20th 2014. Thereafter, a number of manoeuvres will progressively reduce its relative velocity with respect to CG while the SC approaches the nucleus. Several intermediate phases have been devised so that the knowledge of the nucleus' ephemeris, as well as its mass, shape, landmarks, kinematics and gravity potential will be gradually improved.

In November 2014, when the comet heliocentric distance is 3 AU, the Philae lander will separate from the orbiter, following a non-propelled trajectory that will deliver the Surface Science Package to the landing site of choice on the nucleus surface. At this heliocentric distance, nucleus gas activity is still low (mass loss between 2 and 24 kg/s), and nucleus gravity is expected to dominate over the drag force due to the outflowing gas.

Subsequently, while the comet continues its excursion around the Sun, the orbiter will follow it undergoing a number of close fly-bys, during which it is foreseen that the SC will get as close as 5 km from the nucleus centre with relative velocity in the order of 1 m/s. Propellant budget analyses estimate that there will be enough propellant to undertake about 15 close fly-bys before the mission comes to an end. The most severe conditions will be present at perihelion, in mid-August 2015, when the distance between the sun and the comet reaches a minimum of 1.24 AU and the highest gas activity is expected (mass loss in the range 130 to 380 Kg/s). For these levels of activity, gas drag and nucleus gravity are expected to be in the same order of magnitude. The current analysis focuses on this mission phase (the so-called Extended Monitoring Phase) and analyses different methods to predict the drag force on the spacecraft during close fly-bys from data collected during previous fly-bys.

Because it is only possible to perform a few close fly-bys, there will be weeks of separation between two consecutive fly-bys. Hence, coma conditions are expected to change considerably from one fly-by to the next, which suggests the need of incorporating measurements taken by on-board remote sensing instruments into the prediction process.

2. Properties of the Comet Nucleus and the Coma

Comets are small bodies composed out of a mixture of ice and dust particles. When a comet approaches the Sun, its ice starts to sublimate and the sublimated gas drags the dust particles from the surface. This mix of sublimated gas and dust particles constitutes the comet atmosphere (coma) that escapes the vicinities of the comet's nucleus, whose gravitational field is insufficient to retain the atmospheric particles (except for a few very big particles).

The target of Rosetta is comet 67P/Churyumov-Gerasimenko. A shape model of the nucleus was derived by the Laboratoire d'Astrophysique de Marseille from ground-based observations. It consists of a polyhedron of 512 triangular faces and 258 vertices. The overall area of the polyhedron is 41 km^2, equivalent to a sphere of radius 1806 m. As Rosetta approaches the nucleus, this preliminary shape model will be refined from much higher precision in-situ measurements. For our current studies, however, we assume that the nucleus is as described by this preliminary model.

The coma is expected to be mainly composed out of H_2O, CO and CO_2. Minimum and maximum activities for different comet-Sun distances have been estimated from ground-based observations. In particular, at perihelion, a maximum gas activity of 380 kg/s (this includes molecules of H_20, CO and CO_2) with terminal velocity 800 m/s is expected. The dust particles released can cover all possible sizes. The size distribution of those particles has large uncertainties. However it is expected that the overall mass of particles released from the comet is in the same order as that of the gas and that the bulk of the mass of the dust particles is in large particles.

In visual wavelength the spectrum of light emitted by the coma is dominated by light scattered by dust. It is expected that particles larger than 1μm dominate the scattered visual light.

3. Effects of the Coma on the Spacecraft and Coma Observables

Rosetta is a spacecraft composed of a main body (the orbiter) and the Philae lander. The orbiter, stabilized on three-axes, has a roughly cubic shape, with an articulated High Gain Antenna (HGA) on the $+x_{sc}$ face and the solar arrays (SAs) on the $\pm y_{sc}$ faces. The solar arrays can be rotated around the SC y-axis and are always sun pointing. Attitude control in normal mode is performed by means of four reaction wheels, while a system of eight thrusters is used during wheel off-loadings. Other instruments relevant to this study are the navigation cameras (NAVCAMs) with boresight along the SC z-axis and an inertial measurement package that is equipped with accelerometers, that are sensitive to accelerations along any SC axis.

Over the comet dayside the solar arrays dominate the drag force on Rosetta due to their large area (64 m^2). Close to perihelion and over the comet dayside, it is expected that the drag force on Rosetta can be detected directly with the accelerometers. Alternatively, the drag force can be detected by means of the torque exerted on Rosetta. The main contribution to this torque normally comes from the HGA, which has a cross-sectional area of about 4 m^2 and a lever arm of up to 3.6 m (despite the large area of the SAs, they are usually of minor importance for the torque, because the SA centre of pressure is close to the SC centre of mass; note that this also requires that density gradients on the scale of the SC are of minor importance). It is expected that by means of the torque on the SC, the drag can be detected during any phase in the mission. However, a sensitive measurement requires certain articulation angles of the HGA, and this may not be possible always during the mission. Because radiometric data are also affected by gravity, they are not foreseen to be used to measure the drag force.

The comet is expected to release as much gas as dust in terms of mass. However, the bulk of dust mass is expected to be concentrated on large particles, that only reach small velocities relative to the comet. Therefore, the dynamic pressure on the SC is expected to be dominated by the drag exerted by gas. At perihelion, the dominating gas molecule is H_2O. The navigation camera is sensitive to visual wavelength that are dominated by light scattered by dust. Because the NAVCAM can only be used to detect dust remotely, it is being investigated whether the submillimeter channels of Miro [2], that are specifically tuned to detect H_2O remotely, can be used to supplement the NAVCAM measurements.

The aim of this work is to identify different methods for predicting the effect of the coma using the different available measurements. Because it is beyond its scope to analyze the effect of measurement errors, this study uses idealized measurements. Hence it is assumed that for past fly-bys it was possible to measure the acceleration without any error (regardless of which method was used to obtain the measurement). Furthermore, it is assumed that NAVCAM measurements can be reduced to a column density of dust along the line of sight. Analysis has shown that the Miro measurements can be reduced with good accuracy (in the order %) to the gas density at the point of CA along the Miro line of sight. So far no simple method was identified that is able to deduce the column density from Miro with reasonable accuracy.

4. Physical Model of the Coma

Because no measurements of the coma will be available until Rosetta approaches the comet, physical models are used to simulate both the effect of the coma on the SC and the intensities

measured by remote sensing instruments. However, these physical models will not be used for operations. Instead, the approach for prediction will be empirical, i.e. past measurements of the drag force, as well as remote sensing measurements, will be used for predictions under changed geometries and levels of comet activity.

The purpose of this section is to briefly describe the physical models implemented to simulate both the gas and the dust distributions. Because the effect of the dust particles on the dynamics of the gas is negligible, the problem can be decoupled. First, the gas state is determined irrespective of the dust distribution. Only then, the dust distribution can be simulated from the gas state.

4.1. Physical model of the gas

The mix of H_2O, CO and CO_2 is assumed to be in thermal equilibrium and it is assumed that it can be modeled as a single gas species *s* with mass $2.99 \cdot 10^{-26}$ Kg and specific heat ratio 1.33. For each nucleus' triangle, the gas mass flow per unit of surface is set proportional to the scalar product between the triangle normal and the sun direction. A uniform activity is then added to this cosine distribution so that even the shaded portion of the nucleus surface emits some background activity. Only then, the resultant activity distribution is rescaled for consistency with the overall level of activity 380 Kg/s.

For convenience, a *coma reference frame* relative to the sun is defined with origin at the nucleus centre of mass and basis $\{\vec{i}_c, \vec{j}_c, \vec{k}_c\}$ such that $\vec{k}_c$ points in the direction from the Sun to the nucleus centre of mass, $\vec{j}_c$ towards the comet orbital north pole with respect to the Sun and $\vec{i}_c$ completes the frame such that it is right-handed. Spherical coordinates $\{r, \theta, \varphi\}$ are used with the standard convention:

$$x_c = r \sin\theta \cos\varphi \qquad y_c = r \sin\theta \sin\varphi \qquad z_c = r \cos\theta \tag{1}$$

The Euler equation is solved using the Godunov method based on assumed physical parameters on the nucleus surface. The space in the vicinities of the nucleus is covered by a rectangular grid. Boundary conditions are defined on both cells containing a part of the nucleus' surface (inside boundary) and those on the outer walls of the grid (outside boundary).

For the present study, a grid of 56 x 56 x 56 cells of increasing size is defined. The edge size of the smaller cells in the vicinities of the nucleus is 160 m and the grid covers a distance of about 100 km in each direction. The comet attitude and activity is kept constant and the Godunov solver is iterated until a steady state is obtained. For each cell an approximation of the gas state is obtained.

The density and velocity distributions of the state generated with the physical model for the present studies are depicted in Fig. 1 and 3. A significant feature of the gas velocity field is that, after a few transitional kilometers, it converges to a uniform value (about 800 m/s in our model) irrespective of the angle with respect to the subsolar point. This is a consequence of the approximately constant surface temperature on the comet dayside, as will be explained below. Moreover, the gas velocity field is almost radial, with deviations below 5 degrees for distances to the nucleus surface higher than 5 km.

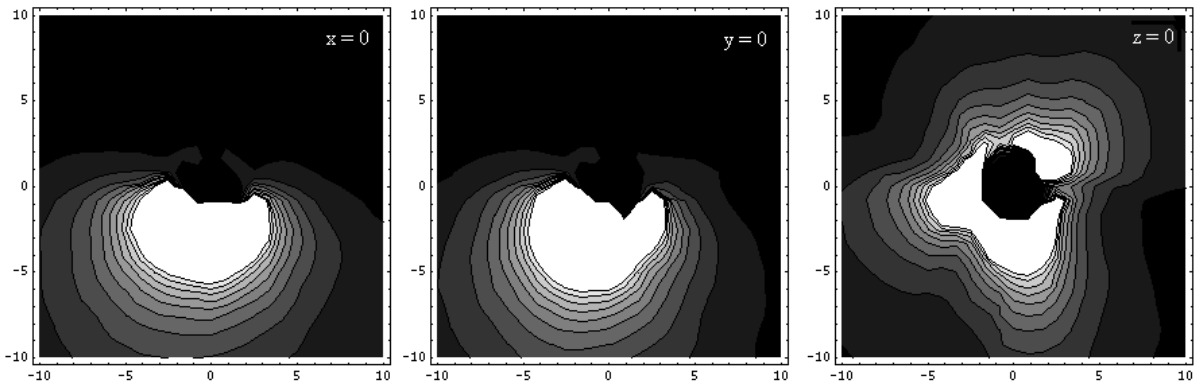

Figure 1. Isodensity lines of physical gas state in coma reference frame. The Sun is located towards $-z_c$, i.e. below the plot for the two first cut-offs and behind the plot for the last one

4.2. Physical model of the dust

The distribution of dust is calculated with a Monte-Carlo simulation. From each face of the nucleus' polyhedron, a large number of dust particles are propagated. For this purpose, the grid defined for the Godunov method is reused. As explained in the previous section, the gas' physical model provides a piece-wise constant estimation of the gas state, i.e. gas state has a constant value in each grid's cell. This gas state is linearly interpolated at each position so that the drag force exerted by the gas on the dust particles can be estimated. Dust particles are assumed to be spherical with drag coefficient equal to 2 and density 1000 Kg/m^3. Moreover, for the sake of simplicity, a single particle size of 10μm is chosen, as it is particles of this size that are thought to dominate the light scattered by the coma. For this particle size, the effect of the gravitational field is negligible and dust particles are propagated assuming that they are only subjected to the drag force of the sublimated gas. The numerical integration of the equation of linear momentum is performed on a cell-by-cell basis, i.e., dust particles' trajectories are propagated inside of each cell until one of the six walls is reached. This way, the time spent by the particle in each cell is known. This cell-by-cell propagation ends when the dust particle reaches the end of the grid.

Once a sufficient number of particles have been propagated from each nucleus' face, the density and average velocity of dust particles in each grid's cell can be estimated from the activity on the nucleus faces, the time spent by the particles in the cell, its average velocity, the volume of the cell and the number of simulated particles per real particle. For the present case, dust activity on the nucleus surface is defined such that the ratio between gas and dust mass flows is uniform and equal to one.

The distribution of density generated with the physical model for dust is depicted in Fig. 2. The fact that there is more structure visible than for the gas is due to the fact that the dust only interacts with the gas in close vicinity, such that inhomogeneities in the density close to the nucleus remain visible at larger distances. Figure 3 highlights another difference between gas and dust states: that the terminal velocity of dust particles tends to be larger the smaller the angle with respect to the subsolar point, whereas it is constant for the gas.

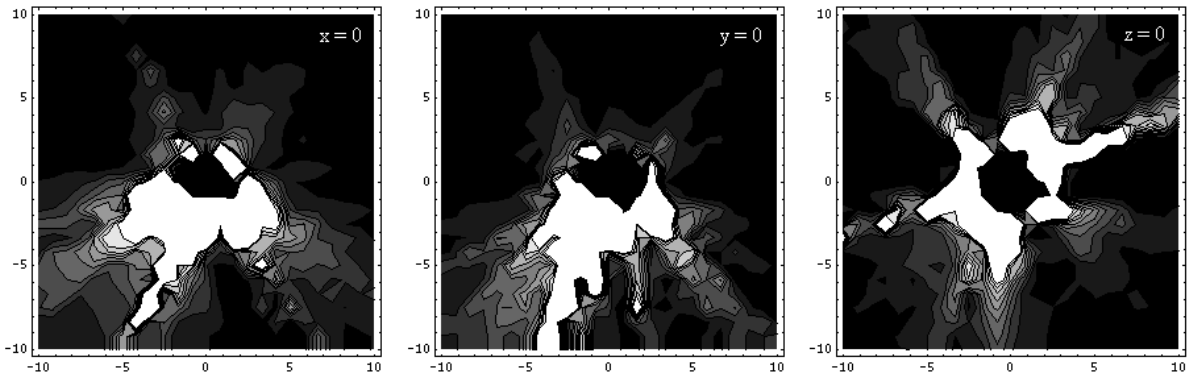

Figure 2. Isodensity lines of physical dust state in coma reference frame. The Sun is located towards $-z_c$, i.e. below the plot for the two first cut-offs and behind the plot for the last one

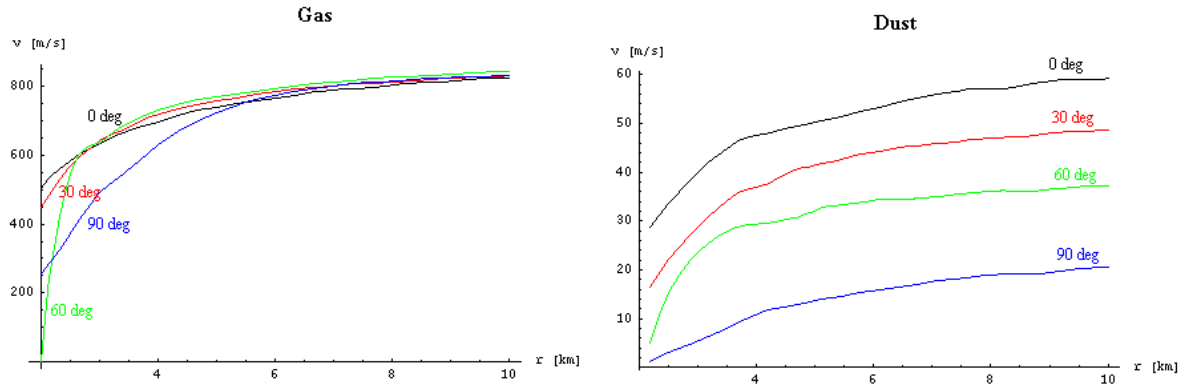

Figure 3. Radial component of gas and dust velocity as read from their physical state. Each line corresponds to a radial trajectory on the plane x_c-z_c. Angles are measured with respect to $-z_c$ (positive rotation about $+y_c$), whereas the horizontal axis is the distance to the nucleus centre.

5. Physical Scaling Laws for the coma

5.1 Velocity of Gas

In the range where Rosetta is operating the gas state is well described by homogenous Euler equations, i.e. external forces, heating and particle dissociations can be neglected. Furthermore, usually the assumption that the gas only interacts along the radial direction relative to some fixed reference point (the centre of the nucleus, in our studies) is a good approximation. Under this condition, the Euler equations for a gas species *s* can be written (see e.g. [1]) as

$$\frac{\partial}{\partial r}(r^2 \rho_s v_s) = 0 \tag{2}$$

$$\frac{\partial}{\partial r}(r^2 \rho_s v_s \eta) = 0 \tag{3}$$

$$\frac{\partial}{\partial(r/r_n)} M_s{}^2 = \frac{2}{(r/r_n)} \frac{M_s{}^2}{M_s{}^2 - 1}\left[(\gamma - 1)M_s{}^2 + 2\right] \tag{4}$$

where r_n is the local nucleus radius [m], ρ_s is the gas density [kg/m^3], v_s is the radial velocity [m/s], r is the distance from the reference point [m], M_s is the Mach number and η is the gas specific enthalpy [J/Kg]. Mach number and enthalpy are given by

$$M_s = \frac{v_s}{\sqrt{\frac{\gamma k T_s}{m_s}}} \quad \text{and} \quad \eta = \frac{1}{2} v_s{}^2 + \frac{\gamma}{\gamma - 1}\frac{k T_s}{m_s} \tag{5}$$

with T_s being the gas temperature [K], m_s the mass of a gas molecule [Kg] and k the Boltzmann constant [J/K].

It is important to note that differential equation Eq. 4 does not depend on the level of activity. Close to the nucleus the Machnumber has a value of 1 and increases strictly monotonically beyond all bounds with increasing distance from the nucleus (which is a direct consequence of the outer boundary condition (expansion into vacuum see [1])). Therefore, assuming that the adiabatic heat ratio is the same everywhere around the comet, the function $M_s(r/r_n)$ is also the same to a good approximation.

Because both $r^2 \rho_s v_s$ and η are constant (Eq. 2 and 3), the density and velocity of the gas can be calculated with help of M_s:

$$\rho_s = \frac{r_{s0}{}^2 v_{s0}}{r^2 v_s} \rho_{s0} \tag{6}$$

$$v_s(r/r_n) = \sqrt{\frac{2(\gamma - 1)M_s(r/r_n)^2 \eta}{(\gamma - 1)M_s(r/r_n)^2 + 2}} \tag{7}$$

Since the Machnumber is approximately one close to the surface it follows that the velocity at the surface is constant for constant enthalpy. Furthermore, from enthalpy conservation it follows that, far away from the nucleus surface, as the gas gets colder, it approaches a terminal velocity $v_{s,\infty}$ given by

$$v_{s,\infty} = \sqrt{2\eta} \tag{8}$$

An implication of this equation is that, if the surface temperature is constant , so is the terminal gas velocity (see Fig.3).

5.2 Velocity of Dust

Dust particles are released from the nucleus surface with null velocity and accelerated by the action of the drag exerted by the gas molecules. The gravitional attraction is only of relevance for the largest particles released from the comet, which are irrelevant to this study. From energy conservation applied to a dust particle:

$$\frac{1}{2} m_d v_d(r)^2 = \int_{r_n}^{r} \vec{F}_{drag} \cdot d\vec{r} \tag{9}$$

with m_d being the mass of the dust particle [Kg] and v_d its velocity [m/s]. The drag force exerted by the gas is

$$\vec{F}_{drag} = \frac{1}{2} c_D A_d \rho_s \left\| \vec{v}_s - \vec{v}_d \right\| \left(\vec{v}_s - \vec{v}_d \right) \tag{10}$$

where c_D is the drag coefficient, A_d its cross-section area [m^2] and $\vec{v}_d$, its velocity vector [m/s]. For $v_s >> v_d$ and assuming that $\vec{v}_s$ goes along the radial direction the drag force is also radial and with norm

$$F_{drag} = \frac{1}{2} c_D A_d \rho_s v_s^2 \tag{11}$$

Now, if $\dot{m}_g$ is the local gas activity on the nucleus surface [Kg/m^2/s], we can write

$$\rho_s v_s r^2 = \dot{m}_s r_n^2 \tag{12}$$

so that

$$\int_{r_n}^{r} \vec{F}_{drag} \cdot d\vec{r} = \frac{1}{2} c_D A_d \dot{m}_s r_n^2 \int_{r_n}^{r} \frac{v_s(r)}{r^2} dr \tag{13}$$

The dependency of the gas velocity on the radial distance is known from Eq. 7, so that the integral on the equation above can be solved and the velocity profile of the dust particles computed. Dust particles reach their terminal velocity $v_{d,\infty}$ within a few nucleus radii (let $r_{d,\infty}$ denote this terminal distance). Thereafter, uniform linear motion sets in.

The integral on the equation above can be computed from the nucleus surface to a point far away from the surface, resulting in

$$\int_{r=r_n}^{\infty} \frac{v_s(r)}{r^2} dr = \frac{2 v_s(r_n) G_\gamma^2}{r_n} \tag{14}$$

Where $G_\gamma \approx 1.4$ for values of γ between 1.33 and 1.4. Finally, the terminal velocity of dust particles released at a given point of the nucleus surface can be computed by

$$v_{d,\infty} = G_\gamma \sqrt{\frac{2 C_D A_d r_n}{m_d} \dot{m}_s v_s(r_n)} \tag{15}$$

Assuming that r_n is constant at different points on the surface (spherical nucleus), and so is the gas velocity (an implication of temperature being approximately constant on the nucleus surface), Eq. 15 implies that the variation of terminal dust velocities over different points of the

nucleus surface is proportional to the square root of the gas activity, that is, for θ and φ being the coordinates defining a point on the nucleus surface, the dependency of the terminal dust velocity on the gas state is simply given by

$$v_{d,\infty}(\theta,\varphi) \propto \sqrt{\dot{m}_s(\theta,\varphi)} \tag{16}$$

This theoretical analysis explains the velocity field depicted in Fig. 3. Indeed, the larger the angle with respect to the sun direction, the lower the level of gas activity and thus the terminal velocity of dust particles.

On a different matter, similar to the case of gas, the radial evolution of dust density can be estimated from mass conservation

$$\rho_d = \frac{r_0^2 v_{d0}}{r^2 v_d}\rho_{d0} \tag{17}$$

Once particles are a few radii away from the nucleus ($r > r_{d,\infty}$) and $v_d \approx v_{d,\infty}$, this relation simplifies to

$$\rho_d \approx \frac{r_0^2}{r^2}\rho_{d0} \tag{18}$$

5.3. Physical Scaling Laws for Density and Velocity

As indicated before, both gas and dust particles reach certain terminal velocities after separating a distance of a few kilometers from the nucleus surface. The existence of such a terminal distance r_∞ is also apparent from Fig. 3. Hence, the state of the gas beyond the terminal distance can be described by

$$\rho_s(r,\theta,\varphi) = \frac{r_\infty^2}{r^2}\rho_s(r_\infty,\theta,\varphi)$$
$$v_s(r,\theta,\varphi) = v_{s,\infty} \tag{19}$$

Similarly, the state of the dust is given by

$$\rho_d(r,\theta,\varphi) = \rho_d(r_\infty,\theta,\varphi)\frac{r_\infty^2}{r^2}$$
$$v_d(r,\theta,\varphi) = v_{d,\infty}(\theta,\varphi) \propto \sqrt{\dot{m}_s(\theta,\varphi)} \tag{20}$$

From Eq. 19 and 20, we can also write (Fig. 4 shows how well this proportionality holds for the numerical model)

$$v_{d,\infty}(\theta,\varphi) \propto \sqrt{\rho_s(r_\infty,\theta,\varphi)} \tag{21}$$

Furthermore, we introduce the assumption that the ratio χ between dust and gas mass flow is the same everywhere on the nucleus surface, that is

$$\dot{m}_d(\theta,\varphi) = \chi\ \dot{m}_s(\theta,\varphi) \tag{22}$$

which leads to

$$\rho_d(r_\infty,\theta,\varphi)v_{d,\infty}(\theta,\varphi) = \chi\ \rho_s(r_\infty,\theta,\varphi)v_{s,\infty} \tag{23}$$

These interrelations between gas and dust states will be extremely useful in our analysis, as they allow us to indirectly derive the effect of the gas drag on the S/C from measurements of the dust. In particular, the following relation can be worked out from the equations above for the gas dynamic pressure at a given position

$$\frac{1}{2}\rho_s(r,\theta,\varphi)v_s(r,\theta,\varphi)^2 \propto \rho_d(r,\theta,\varphi)\sqrt{\rho_s(r_\infty,\theta,\varphi)} \tag{24}$$

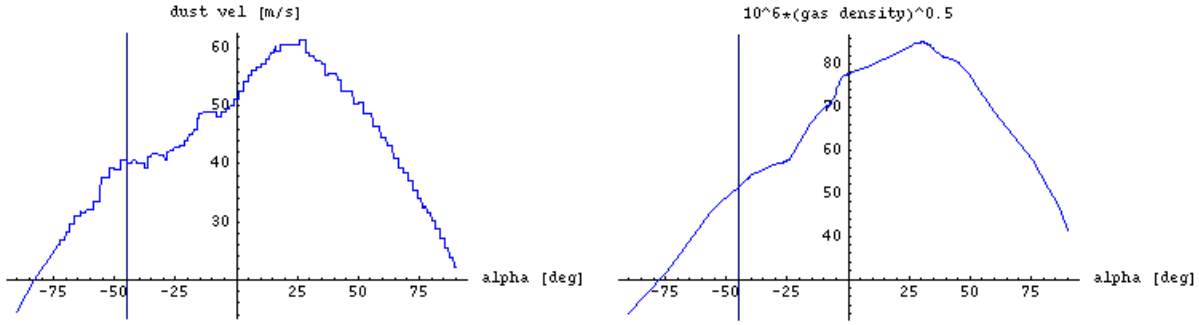

Figure 4. Profile of dust velocity (left) and a factor of the square root of the gas density (right) for different values of α and distance to the nucleus centre 5 km

6. Methods for prediction of coma drag force on Rosetta during a fly-by

For this study, it is assumed that during a fly-by, the SC follows a uniform linear motion with relative velocity to the nucleus $\vec{v}_{SC}$ of norm 1 m/s and direction $\vec{u}_v$. Let $\vec{d}$ denote the vector from the nucleus centre to the point of closest-approach (CA), with norm d and direction $\vec{u}_d$. Also, for convenience, let us define a Cartesian fly-by reference frame with the basis $\{\vec{u}_n,\vec{u}_v,\vec{u}_d\}$, with $\vec{u}_n = \vec{u}_v \times \vec{u}_d$, and origin in the nucleus centre. The SC position is given by

$$\vec{r}(\alpha) = d\vec{u}_d + (d\tan\alpha)\vec{u}_v \tag{25}$$

where α is the angle of the SC from closest-approach and $\tan\alpha = s/d$ (see Fig. 5) with s the distance of the SC from CA, i.e. $s = \vec{r}\cdot\vec{u}_v$. A last parameter defined now for convenience is η: the angle between $\vec{d}$ and the sun direction relative to the nucleus, $\vec{u}_{sun}$.

Figure below depicts all parameters described so far.

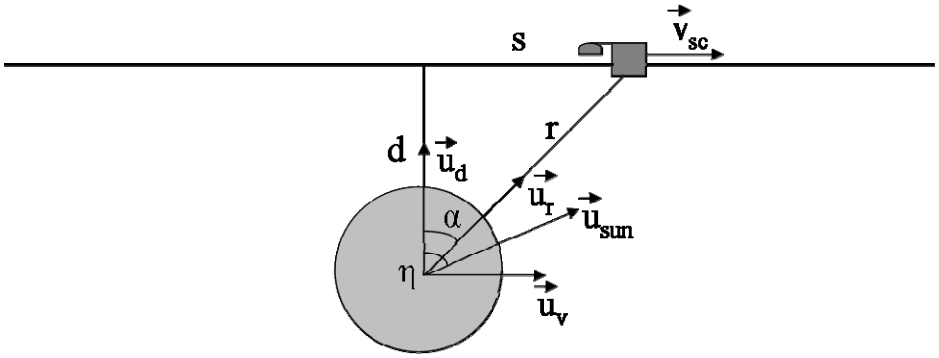

Figure 5. Parameters of a generic fly-by trajectory in fly-by frame

Assuming that the interaction between the coma gas molecules and the SC's surface is perfectly inelastic, the drag acceleration of the SC at a given time can be written as

$$\vec{a}_{drag} = \frac{1}{2}\frac{c_D A_{SC}\rho_s}{m_{SC}}\left\|\vec{v}_s - \vec{v}_{SC}\right\|\left(\vec{v}_s - \vec{v}_{SC}\right) \tag{26}$$

with A_{sc} being the cross-sectional area of the SC towards the flow [m^2] (function of the flow direction, the SC attitude and the articulation angles of both SAs and HGA), $\vec{v}_{SC}$, the velocity of the SC relative to the nucleus [m/s], m_{SC}, the SC mass [Kg] and c_D, the SC's coefficient of drag, equal to 2 (free molecular regime).

Because the gas reaches supersonic velocities, much larger than the SC velocity, $\vec{v}_s - \vec{v}_{SC} \approx \vec{v}_s$. Furthermore, assuming gas interaction is constrained to the radial direction, the drag force acts along the radial direction $\vec{u}_r = \vec{r}/r$ and the acceleration due to drag can be predicted by

$$\vec{a}_{drag}(\alpha) \approx \frac{1}{2}\frac{c_D A_{SC}(\alpha)\rho_g(\alpha)}{m_{SC}} v_s(\alpha)^2 \vec{u}_r(\alpha) \tag{27}$$

Now, given two fly-bys: one during which the acceleration is measured (denoted by subscript m) and another for which the acceleration is predicted (subscript p), and assuming once again that the gas only interacts along the radial direction, the equation above leads to the acceleration prediction

$$\vec{a}_p(\alpha) = \frac{\rho_p(\alpha)}{\rho_m(\alpha)}\frac{v_p(\alpha)^2}{v_m(\alpha)^2}\frac{A_p(\alpha)}{A_m(\alpha)}\left(\vec{a}_m(\alpha)\cdot\vec{u}_{r,m}(\alpha)\right)\vec{u}_{r,p}(\alpha) \tag{28}$$

where, for each fly-by, the angle α is defined with respect to the closest-approach direction of each of the fly-bys, i.e. $a_p(\alpha)$, $\rho_p(\alpha)$, $v_p(\alpha)$, $A_p(\alpha)$ and $\vec{u}_{r,p}(\alpha)$ are given at the point of fly-by p where the S/C relative position forms an angle α with respect the CA direction of fly-by p, whereas $a_m(\alpha)$, $\rho_m(\alpha)$, $v_m(\alpha)$, $A_m(\alpha)$ and $\vec{u}_{r,m}(\alpha)$ are given at the point of fly-by m where the SC relative position forms an angle of α with respect to the closest-approach direction of fly-by m.

Note that the errors on the acceleration prediction $\vec{a}_p(\alpha)$ come for three different sources:

1. Errors in the measurement of $\vec{a}_m(\alpha)$.
2. Errors in the assumptions done to derive Eq. 28: negligible dust drag force, gas only acts along the radial direction relative to the nucleus centre, inelastic collision of the gas molecules with the SC, etc.
3. Errors in the estimation of each of the three ratios of Eq. 28.

In addition to the assumption of error-free availability of both $\vec{a}_m(\alpha)$ and remote measurements, in order to further focus our analysis, at this point we assume:

1. Null drag force due to dust.
2. Perfectly inelastic collisions between the gas molecules and the SC.
3. Perfect knowledge of the SC geometry, attitude, and HGA and SAs angles, i.e. no error in the estimation of $A(\alpha)$.

This means that the errors committed in our analysis will be solely due to:

1. Errors in the estimation of the ratios $\rho_p(\alpha)/\rho_m(\alpha)$ and $v_p(\alpha)/v_m(\alpha)$.
2. Error derived from the assumption that the gas velocity is radial with respect to the nucleus centre. For the physical gas state, at distances from the nucleus centre larger than 5 km, gas deflection is always below 5 degrees, which translates into negligible errors below 0.4%.

In the following, we present a number of methods developed to predict the ratios $\rho_p(\alpha)/\rho_m(\alpha)$ and $v_p(\alpha)/v_m(\alpha)$ for different sets of available input measurements. Later, we will assess the accuracy of these methods by predicting, from measurements derived from the physical models of gas and dust, the drag that the coma would exert on the SC, was the gas state identical to that of the physical model. We will do this for a number of simple fly-by geometries in order to assess the strengths and flaws of each method. Furthermore, in order to simplify the expressions of the prediction methods, both the SC attitude and the SAs and HGA rotation angles will be identical at equivalent points of different fly-bys, so that $A_p(\alpha)/A_m(\alpha)=1$ in Eq. 28 (the accuracy of the shape model of Rosetta is out of the scope of this paper).

6.1 R-squared scaling

The first scenario is: provided the acceleration profile $\vec{a}_m(\alpha)$ during an initial fly-by, estimate the acceleration profile $\vec{a}_p(\alpha)$ during a second fly-by in the absence of remote measurements. Because there is no information about possible changes in comet activity between one fly-by and the other, all we can do is to use the analytical expressions for the gas dynamics. Since using Eq. 7 to scale down gas velocities from an outer fly-by to an inner one may lead to very large errors (because of the shape of the curve in Figure 3), it is preferable to assume that $v_p(\alpha)/v_m(\alpha)=1$. This results in simple r-square scaling $\rho_p(\alpha)/\rho_m(\alpha)=r_m(\alpha)^2/r_p(\alpha)^2$ so that the acceleration of fly-by p can be predicted by:

$$\vec{a}_{\mathrm{p}}(\alpha) = \frac{\mathrm{r_m}(\alpha)^2}{\mathrm{r_p}(\alpha)^2}(\vec{a}_m(\alpha)\cdot\vec{u}_{r,m}(\alpha))\vec{u}_{r,p}(\alpha) \tag{29}$$

Although the predictions from the R-squared scaling will be very poor when either fly-bys have very different angles η or changes in nucleus activity from one fly-by to the other are significant, this is the best possible scaling in the absence of remote-sensing measurements.

6.2 CA-density scaling

Now we assume that not only $\vec{a}_m(\alpha)$, but also gas densities at the closest-approach positions of fly-bys m and p are known (expected to be available from Miro, see section 3). They are respectively denoted by $\rho_{s,m}(\vec{d}_m)$ and $\rho_{s,p}(\vec{d}_p)$. We can now replace the R-squared scaling of the preceding method by the ratio of densities actually measured at CA

$$\vec{a}_{\mathrm{p}}(\alpha) = \frac{\rho_{s,p}(\vec{d}_p)}{\rho_{s,m}(\vec{d}_m)}(\vec{a}_m(\alpha)\cdot\vec{u}_{r,m}(\alpha))\vec{u}_{r,p}(\alpha)\,. \tag{30}$$

This method should represent an improvement over the simple R-square scaling when either angle η or the activity profile changes significantly from one fly-by to the other.

6.3 Gas column density scaling

This time, we assume that in addition to $\vec{a}_m(\alpha)$, there is at our disposal a measurement I proportional to the gas column density along the fly-by trajectory for both fly-bys m and p (I_m and I_p, respectively). Assuming, for the sake of simplicity, that I is not only proportional to, but actually equal to the column density, its value is given by

$$I = \int_{s_0}^{\infty} \rho_s(s)ds \tag{31}$$

with units Kg/m^2. We can re-write

$$I = \frac{1}{d}\int_{\alpha_0}^{\pi/2} \rho_s(\alpha)r(\alpha)^2\,d\alpha = \frac{1}{d}\int_{\alpha_0}^{\pi/2} \rho_s(\alpha)r(\alpha)^2 v_s(\alpha)\frac{1}{v_s(\alpha)}d\alpha \tag{32}$$

But from Eq. 6 we know that for two fly-bys with same η and gas distribution, $\rho_s(\alpha)r(\alpha)^2 v_s(\alpha)$ is approximately the same for all α. Thus, for $\bar{v}_{s,m}$ and $\bar{v}_{s,p}$ being some average gas velocity during fly-bys m and p, we can write

$$I_p d_p \bar{v}_{s,p} \approx I_m d_m \bar{v}_{s,m} \tag{33}$$

If we further assume once more a velocity ratio of one, the equation above simplifies to

$$I_p d_p \approx I_m d_m \tag{34}$$

On what follows, we will refer to the magnitude $I^c = I\ d$ as *corrected gas column density*.

Finally, the acceleration of fly-by p can be predicted by:

$$\vec{a}_{\mathrm{p}}(\alpha) = \frac{\mathrm{r_m}(\alpha)^2}{\mathrm{r_p}(\alpha)^2} \frac{I_p^c}{I_m^c} (\vec{a}_m(\alpha) \cdot \vec{u}_{r,m}(\alpha)) \vec{u}_{r,p}(\alpha) \tag{35}$$

This prediction method can be understood as an enhancement of the R-squared scaling that will return better estimates whenever either η or the gas state changes significantly from one fly-by to the other, but only at the expense of a method-intrinsic error of magnitude

$$\varepsilon_s = \left| \frac{I_p^c}{I_m^c} - 1 \right| \tag{36}$$

for $\eta = 0$ and unchanged gas activity, mainly derived from the fact that the gas velocity does not remain constant, but in fact increases as the gas expands, as predicted by Eq. 7 and depicted in Fig. 3.

6.4 Dust column density scaling

The inputs for this method are similar to those for the gas-column-density-scaling, just that this time the available column density along the fly-by direction is not that of a gas species, but of dust particles. (from NAVCAM, see section 3). Thus, dust column density along the fly-by direction is given by

$$J = \int_{s_0}^{\infty} \rho_d(s) ds \tag{37}$$

with units Kg/m^2. The same computations that were done for the gas column density can now be done for the dust arriving at

$$J_p d_p \bar{v}_{d,p} \approx J_m d_m \bar{v}_{d,m} \tag{38}$$

and again this expression can be further simplified by assuming $\bar{v}_{d,p} \approx \bar{v}_{d,m}$ so that

$$J_p d_p \approx J_m d_m \tag{39}$$

From now, we will refer to the magnitude $J^c = J\ d$ as *corrected dust column density*.

Nevertheless, because the drag force on the SC is provoked not by the dust, but by the gas molecules, this is a more indirect method that can only be expected to work under the additional assumption that the ratio χ between dust and gas mass flow is always and everywhere the same, that is

$$\dot{m}_d(\theta, \varphi, t) = \chi\ \dot{m}_s(\theta, \varphi, t) \quad \forall \theta \in [0, \pi], \varphi \in [0, 2\pi), t \tag{40}$$

All in all, the equation of the dust-column-density-scaling prediction method is

$$\vec{a}_{\mathrm{p}}(\alpha) = \frac{\mathrm{r_m}(\alpha)^2}{\mathrm{r_p}(\alpha)^2} \frac{J_p^c}{J_m^c} (\vec{a}_m(\alpha) \cdot \vec{u}_{r,m}(\alpha)) \vec{u}_{r,p}(\alpha) \tag{41}$$

and similarly to Eq. 36, the method introduces an intrinsic error that in the case of $\eta = 0$ and unchanged gas distribution between the two fly-bys is given by

$$\varepsilon_d = \left| \frac{J_p^c}{J_m^c} - 1 \right| \tag{42}$$

6.5 Dust column density scaling with correction for dust velocity

Because after a few kilometers, dust particles have already been accelerated up to their terminal velocity, and this terminal velocity is a function of the gas activity at every point on the nucleus surface, the assumption $\bar{v}_{d,p} \approx \bar{v}_{d,m}$ will lead to very poor predictions with the column-density-scaling method whenever fly-bys m and p have very different η. However, some information about the gas activity can be inferred from the gas density at the point of closest-approach, which in theory will allow us to improve the predictions of the dust-column-density-scaling method by incorporating information on the difference of dust particles velocity between one fly-by and the other.

Let us choose as typical dust velocities during the fly-bys $\bar{v}_{d,m}$ and $\bar{v}_{d,p}$ those at the CA point of each fly-by. At this distance from the nucleus surface, we assume that gas velocities have already converged to their terminal values, so that, from Eq. 12 and 16, the ratio of dust velocities is given by

$$\frac{\bar{v}_{d,p}}{\bar{v}_{d,m}} \approx \sqrt{\frac{\dot{m}_{s,p}}{\dot{m}_{s,m}}} \approx \sqrt{\frac{\rho_{s,p}(\vec{d}_p)}{\rho_{s,m}(\vec{d}_m)}}\frac{d_p}{d_m} \tag{43}$$

where $\rho_{s,m}(\vec{d}_m)$ and $\rho_{s,p}(\vec{d}_p)$ denote the gas density at the point of CA for fly-bys m and p, respectively.

By scaling now with Eq. 38 instead of Eq. 39, we arrive at the final equation

$$\vec{a}_{\mathrm{p}}(\alpha) = \frac{\mathrm{r_m}(\alpha)^2}{\mathrm{r_p}(\alpha)^2}\frac{J_p^c}{J_m^c}\frac{d_p}{d_m}\sqrt{\frac{\rho_{s,p}(\vec{d}_p)}{\rho_{s,m}(\vec{d}_m)}}(\vec{a}_m(\alpha)\cdot\vec{u}_{r,m}(\alpha))\vec{u}_{r,p}(\alpha) \tag{44}$$

Now the method-intrinsic error for unchanged η and coma state is

$$\varepsilon_{d,c} = \left|\frac{J_p^c d_p\sqrt{\rho_{s,p}(\vec{d}_p)}}{J_m^c d_m\sqrt{\rho_{s,m}(\vec{d}_m)}} - 1\right| \tag{45}$$

This method is from now also referred to as *corrected-dust-column-density-scaling*.

6.6 Local density scaling from LS fit from gas

At this point we are going to assume that we have availability of not just a column density measurement along a certain direction, but a whole set of images of the gas from several points of view. For each of these images, the intensity at each point on the image plane is proportional to the gas column density along the direction of the line of sight. The approach now is to define a distribution of gas density with the whole set of spherical harmonics up to order one and a radial dependency inversely proportional to r^2, that is

$$\rho_s^{LS}(r,\theta,\varphi) = \frac{1}{r^2}\left[a_s + b_s\sin\theta\cos\varphi + c_s\sin\theta\sin\varphi + d_s\cos\theta\right] \tag{46}$$

and fit the set of coefficients $\{a_s, b_s, c_s, d_s\}$ with the column density information contained on the images by means of the least-squares method (LS). The convention used for the spherical coordinates is as given by Eq. 1.

Three features of this distribution function are worth a comment:

1. The density distribution is an axial-symmetric cos-distribution wrt. direction $\{b_s, c_s, d_s\}$.
2. The assumption of inverse dependency on r-squared comes again from the assumption that gas velocity remains constant for different radial distances, which will introduce some intrinsic errors.
3. The quality of the fit depends on the point from which the images are taken. This is illustrated in Fig. 6, that displays the propagation of gas coming from two different directions with respect to the subsolar direction $-z_c$. Assuming the dependency of the density on the distance to the nucleus centre is known (inverse r-squared), there is only a degree of freedom θ left. Hence, it may be possible to derive the distribution of density from a single image. That is the case when the observer is located far away from the nucleus in a direction perpendicular to $-z_c$. This can be easily understood in the two-cone-surfaces model of the picture: first, one can derive the density for the outer cone surface and only then subtract the contribution of the outer cone surface to the column density at a θ equal to that of the inner cone surface so as to calculate the density on the inner cone surface. Contrariwise, an observer located at $-z_c$ can not derive any information whatsoever as of the density distribution, as it is not possible for him to isolate the contribution of the different cone surfaces.

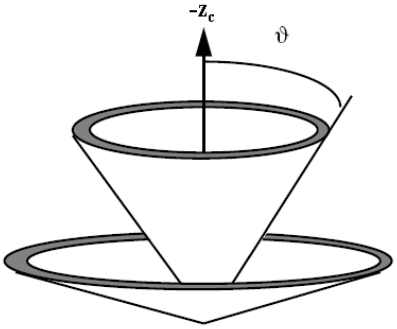

Figure 6. Cone surfaces of gas coming from two different directions for an axial-symmetric coma

Now, for a real-life 3-dimensional coma (albeit still assuming inverse r-square dependency), the number of degrees of freedom increases to two (θ and φ), which requires an infinite number of images in order to derive the distribution of density. In practice, this brings about the fundamental implication that the knowledge of the distribution of density will always be incomplete, not only because of real-life effects, but because of the very nature of the problem. But although incomplete, its degree of completeness will still depend on the adequacy of the selection of viewpoints for the images. One can understand intuitively that again an observer located along a direction perpendicular to $-z_c$ will collect more valuable information than one located along $-z_c$. For each image, it is possible to select different

regions of data to feed into the LS fit, and an adequate alignment between the selection of these regions and the space where the fit is going to be used is another critical determinant of the quality of the fit. In our studies, we will work with only two images taken from points perpendicular to $-z_c$, and will select the semi-plane of the image towards the sun direction to feed the LS fit. Gas density will be taken as null whenever the resultant function $\rho_s^{LS}(r,\theta,\varphi)$ would have provided a negative value.

Once the coefficients of $\rho_s^{LS}(r,\theta,\varphi)$ are computed with the least-squares method, it is possible to predict the acceleration profile of fly-by p from that of fly-by m by

$$\vec{a}_{\mathrm{p}}(\alpha)=\frac{\rho_s^{LS}(\vec{r}_{\mathrm{p}}(\alpha))}{\rho_s^{LS}(\vec{r}_{\mathrm{m}}(\alpha))}(\vec{a}_m(\alpha)\cdot\vec{u}_{r,m}(\alpha))\vec{u}_{r,p}(\alpha) \tag{47}$$

where $\rho_s^{LS}(\vec{r}_{\mathrm{p}}(\alpha))$ and $\rho_s^{LS}(\vec{r}_{\mathrm{m}}(\alpha))$ are the densities provided by the fit at the points of the trajectories that form an angle α with respect to, respectively, $\vec{d}_{\mathrm{p}}$ and $\vec{d}_{\mathrm{m}}$.

This method is from now also referred to as *local-gas-density-scaling*.

6.7 Local density scaling from LS fit from dust

This method is similar to that of the gas, but this time the coefficients of a function

$$\rho_d^{LS}(r,\theta,\varphi)=\frac{1}{r^2}\left[a_d+b_d\sin\theta\cos\varphi+c_d\sin\theta\sin\varphi+d_d\cos\theta\right] \tag{48}$$

are fitted to approximate the density distribution of dust. Assuming again constant dust to gas ratio χ, the equation of prediction is now

$$\vec{a}_{\mathrm{p}}(\alpha)=\frac{\rho_d^{LS}(\vec{r}_{\mathrm{p}}(\alpha))}{\rho_d^{LS}(\vec{r}_{\mathrm{m}}(\alpha))}(\vec{a}_m(\alpha)\cdot\vec{u}_{r,m}(\alpha))\vec{u}_{r,p}(\alpha) \tag{49}$$

This method is from now also referred to as *local-dust-density-scaling*.All remarks about coma observability and the quality of the least-squares fit done in the preceding section remain valid.

6.8 Local density scaling from LS fit from gas with correction for actual density at CA

When the LS fit of gas is done using a wide range of data from the images, the distribution of density $\rho_s^{LS}(r,\theta,\varphi)$ can deviate substantially from the actual density at certain locations. Because most of the interaction between the coma and the SC takes place around the CA position, deviations in the fit from the actual density about the CA position will lead to poor estimations of the overall effect of the coma on the SC. There are two ways to improve the prediction:

1. Reduce the range of data of the LS fit to a region around the CA position.
2. Incorporate estimations of the gas densities at CA into the local-dust-density-scaling formula, resulting in

$$\vec{a}_{\mathrm{p}}(\alpha)=\frac{\rho_s^{LS}(\vec{r}_{\mathrm{p}}(\alpha))}{\rho_s^{LS}(\vec{r}_{\mathrm{m}}(\alpha))}\frac{\rho_{s,p}(\vec{d}_p)}{\rho_{s,m}(\vec{d}_m)}\frac{\rho_s^{LS}(\vec{d}_m)}{\rho_s^{LS}(\vec{d}_p)}(\vec{a}_m(\alpha)\cdot\vec{u}_{r,m}(\alpha))\vec{u}_{r,p}(\alpha) \tag{50}$$

This method is from now also referred to as *corrected-local-gas-density-scaling*.

6.9 Local density scaling from LS fit from dust with correction for dust velocity

The prediction formula given by Eq. 49 assumes that gas dynamic pressure is proportional to dust density. However, according to Eq. 24, this is not the case at points with different gas activity. Hence, as it was done in the corrected-dust-column-density-scaling method, we can enhance the prediction by incorporating information on gas density at CA. Applying Eq. 24 at closest-approach positions (we cannot apply it everywhere along the trajectory as we only know gas density at the points of CA), we end up in the expression

$$\vec{a}_{\mathrm{p}}(\alpha) = \frac{\rho_d^{\,LS}(\vec{r}_{\mathrm{p}}(\alpha))}{\rho_d^{\,LS}(\vec{r}_{\mathrm{m}}(\alpha))} \sqrt{\frac{\rho_{s,p}(\vec{d}_p)}{\rho_{s,m}(\vec{d}_m)}} \frac{d_p}{d_m} (\vec{a}_m(\alpha) \cdot \vec{u}_{r,m}(\alpha)) \vec{u}_{r,p}(\alpha) \tag{51}$$

This method is from now also referred to as *corrected-local-dust-density-scaling*.

7. Simulation exercise

The physical model for gas introduced in section 4.1 is used in order to generate actual acceleration profiles $\vec{a}_m(\alpha)$ to take as reference for later predictions and also to assess the accuracy of those later predictions $\vec{a}_{\mathrm{p}}(\alpha)$ with the scaling methods presented in the preceding section. Furthermore, the physical models of both gas and dust are used to derive the error-free measurements used as input by the different scaling methods.

The accuracy of the drag predictions is established with reference to both plots of predicted versus actual acceleration and the relative error in the prediction of $\Delta\vec{v}$ (time in days, velocity in m/s), calculated as

$$\Delta\vec{v} = 86400 \int_{t_i}^{t_f} \vec{a}(t) dt \tag{52}$$

Note that $\Delta\vec{v}$ is simply a measure of the magnitude of the integral effect of the coma on the SC, as opposed to the actual delta-V, since the trajectory is maintained linear in spite of the drag force.

We now first define the fly-by cases that will be used for our analyses, and then present and discuss the results.

7.1 Description of cases

Three fly-by linear trajectories with uniform motion contained on the plane perpendicular to $\vec{u}_n$ are defined in the table below

Table 1. Description of fly-by cases

	Case 1	Case 2	Case 3
Distance d	10 km	5 km	5 km
Angle η	0 deg	0 deg	45 deg

Because the focus of the study is on the prediction of the gas dynamic pressure, as opposed to its interaction with the SC (dependence on its shape, mass and surface properties), a simple common profile has been selected for the three fly-by cases:

- constant attitude with z_{sc} pointing towards the nucleus centre at the closest-approach position
- constant rotation angles of SAs, with solar cells pointing towards $-z_{sc}$
- constant rotation angles of HGA, with the boresight pointing towards z_{sc}

Although unrealistic (with this profile some SC constraints regarding sun illumination would not be fulfilled), this profile maximises the force exerted by the gas on the SC at CA, by maximizing the SC cross section area to a value of 72.619 m^2 at the point where the distance to the nucleus surface is minimum.

Fly-by case 1 will be used as reference case for predictions of both cases 2 and 3. Case 2 is also used as reference for predictions of case 3. While predictions of case 2 from case 1 are used to assess the behaviour of the different prediction methods in the face of changed CA distances, predictions of case 3 from case 2 isolate the effect of differences in the angle with respect to sun direction. In fact, case 3 can also be understood as a case with identical geometry to case 2 but in the presence of an instable coma that changes its activity profile from one fly-by to the other (in this case, the change is such that the point of maximum activity on the nucleus surface is tilted 45 degrees). Finally, predictions of case 3 from case 1 account for differences on both distances and angles relative to the sun.

For case 1, the fly-by trajectory starts 24 hours before perihelion time and ends after another 24 hours, i.e. the fly-by lasts 48 hours during which the SC advances 172 km. For cases 2 and 3, the initial position and time are defined such that the initial angle α is the same as for case 1 and again the SC reaches its CA position at perihelion time, i.e. fly-bys 2 and 3 last 24 hours during which the SC covers a distance of 86 km.

The following table provides information about gas and dust state at the closest-approach positions of the three fly-bys. These numbers will be useful for understanding the errors derived from the different prediction methods.

Table 2. Gas and dust state at CA positions

	Case 1	Case 2	Case 3
Gas density at CA	$1.26 \cdot 10^{-9}$ Kg/m^3	$6.03 \cdot 10^{-9}$ Kg/m^3	$2.66 \cdot 10^{-9}$ Kg/m^3
Gas radial velocity at CA	824.94 m/s	740.07 m/s	761.44 m/s
Dust density at CA	$5.10 \cdot 10^{-9}$ Kg/m^3	$1.18 \cdot 10^{-8}$ Kg/m^3	$9.81 \cdot 10^{-8}$ Kg/m^3
Dust radial velocity at CA	58.89 m/s	50.70 m/s	39.87 m/s

At a first glance, it might seem surprising that dust density at CA is higher for case 3 than for case 2, but this peak of density can actually be observed in Fig. 2 and comes from the fact that the nucleus surface presents a concavity around that angular position. Because of the higher dust density, dust velocity is lower at the CA of case 3 than at the CA of case 2. This is consistent with the gas state, since gas density at the CA of case 2 is higher than gas density at the CA of case 3 (as we would expect from Eq. 21). From Fig. 2, note that on the semi-plane $y_c=0$, $x_c>0$ the dust state is much more regular. The closest-approach position of fly-by 3 is however on $y_c=0$, $x_c<0$, and the irregular dust state makes the prediction even more challenging.

Table 3 collects the values of the gas and dust corrected column density measurements used for the different fly-by cases:

Table 3. Gas and dust state at CA positions

	Case 1	Case 2	Case 3
Corrected gas column density (I^c)	0.2415 Kg/m	0.2788 Kg/m	0.2069 Kg/m
Corrected dust column density (J^c)	3.653 Kg/m	3.594 Kg/m	3.285 Kg/m

7.2 Results and remarks

In this section, we provide tables and figures with the results of the simulation exercise, and analyze those results. The tables bring together the prediction errors for all combinations of cases and methods in terms of $\Delta\vec{v}$. Column Δv contains the norm of $\Delta\vec{v}$, whereas column "Error Δv (%)" is defined as 100 times the norm of the vectorial difference between the predicted and the actual value divided by the norm of the actual value. In addition, one set of figures is provided for each fly-by case. Each figure shows the actual and predicted acceleration profiles (the former in black and the latter in blue color) in m/s^2 with respect to time. Time is given in hours, relative to CA time.

7.2.1 Predictions of case 2 from case 1

The simple R-squared method provides surprisingly good predictions with errors below 5%. This error originates in fact from two main different sources:

- the fact that, for each α, gas velocity is higher for fly-by 1 than for fly-by 2 (we are assuming the ratio of velocities to be one)
- the fact that, for each α, the ratio of gas densities between fly-bys 1 and 2 is not ¼, as the method assumes in this case

Looking at the gas state, the R-squared method underestimates density by about 17% throughout the fly-by, but this error is counteracted by an overestimation of the squared-velocity by about 20%, which results in the overall overestimation of less than 5%. Nonetheless, had the profile of nucleus activity been defined in a different way, the prediction would have been much less impressive, as errors would not have compensated one another.

This is exactly what happens with the CA-density-scaling method, for which the overestimation of squared-velocity is not offset by a significant error in densities, resulting in an overall error over 20%.

On the other hand, since both η and the activity profiles are the same for fly-bys 1 and 2, the gas-column-density-scaling method does not contribute much, and instead adds up the intrinsic error given by Eq. 36, leading to an overall estimation error of over 18%.

The intrinsic error of the dust-column-density-scaling, however, happens to be much smaller in this case (because J^c is similar for cases 1 and 2) and thus, although it does not incorporate valuable information, it does not introduce a large intrinsic error either, amounting to an overall estimation error of about 4%.

For the least-square fit of the gas state, two images taken from 250 km away from the nucleus are used, one from $+x_c$ and another from $+y_c$, so as to minimise observability issues. The fit generates the following coefficients for Eq. 46: $\{a_s, b_s, c_s, d_s\}$ = {0.0227969, 0.0215850, 0.0203263, 0.108314} Kg/m, which corresponds to an axial-symmetric fit with respect to axis {0.19221, 0.181002, 0.964517}, which happens to be tilted 15.31 degrees with respect to the sun direction. The figure below shows actual versus predicted densities with the LS fit.

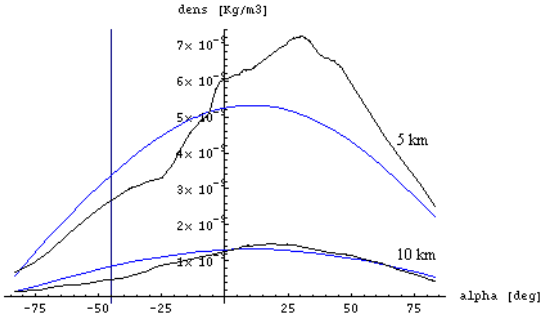

Figure 7. Actual gas density (black) vs gas density predicted by the LS fit (blue) along two circles at 5 and 10 km from the nucleus centre

The same two points of view are used for the images of the dust state. This time, the fit generates the coefficients for Eq.48: $\{a_d, b_d, c_d, d_d\}$= {0.413844, 0.486841 , 0.0343628 , 1.57158} Kg/m, which corresponds to an axial-symmetric fit with respect to axis {0.295841, 0.0208814, 0.955009}, which happens to be tilted 17.25 degrees with respect to the sun direction and 10.96 degrees with respect to the symmetric axis of the gas fit.

However, as both the gas function Eq. 46 and the dust function Eq. 48 assume inverse R-squared dependency and for each α, the value of θ and φ is the same for fly-by cases 1 and 2, it turns out that both the gas- and dust-local-density-scaling methods are equivalent to the R-squared-scaling method for this particular case. Moreover, the corrected-gas-local-density-scaling is in this case equivalent to the CA-density-scaling. The corrected-dust-local-density-scaling, however, incorporates the factor

$$\sqrt{\frac{\rho_{s,p}(\vec{d}_p)}{\rho_{s,m}(\vec{d}_m)}}\,\frac{d_p}{d_m}$$

which increases the error to to 13%.

Table 4 provides the actual value of Δv for fly-by case 1, and Tab. 2, both the actual and predicted values for fly-by case 2.

Table 4. Actual values for case 1 (reference case)

	Δv [m/s]
Actual values	0.56767

Table 5. Estimations for case 2 from case 1

Method	Δv [m/s]	Error Δv (%)	Method	Δv [m/s]	Error Δv (%)
Actual values	1.1192	-	R-squared scaling	1.1442	4.68%
CA-density scaling	1.3714	22.98%	Gas column density scaling	1.3213	18.59%
Dust column density scaling	1.1255	4.11%	Corrected dust column density scaling	1.2322	10.96%
Gas local density scaling	Equivalent to R-squared scaling		Corrected gas local density scaling	Equivalent to CA-density scaling	
Dust local density scaling	Equivalent to R-squared scaling		Corrected dust local density scaling	1.2527	12.68%

Actual (black) vs predicted acceleration (blue) for case 2 from data for case 1

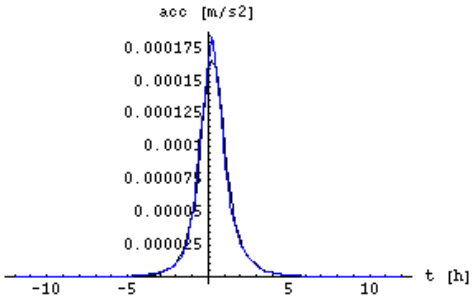

Figure 8. R-squared scaling

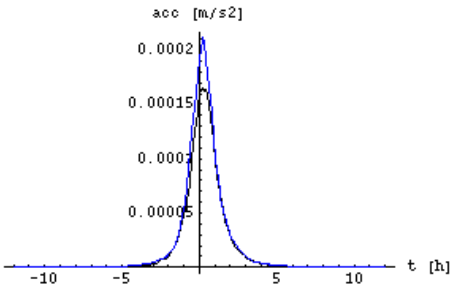

Figure 9. Gas column density scaling

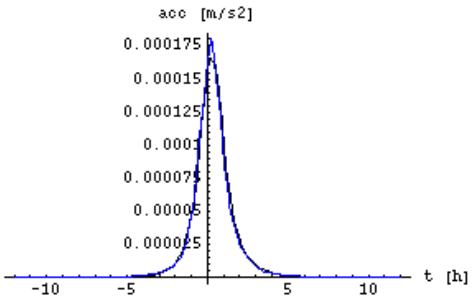

Figure 10. Dust column density scaling

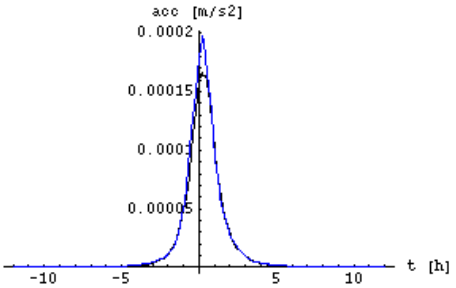

Figure 11. Corrected dust column density scaling

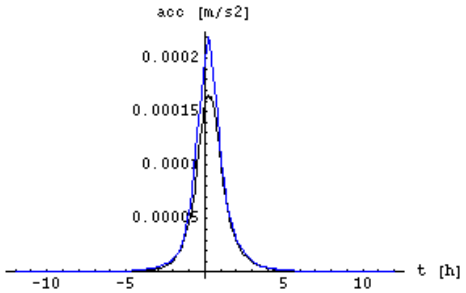

Figure 12. Corrected gas local density scaling

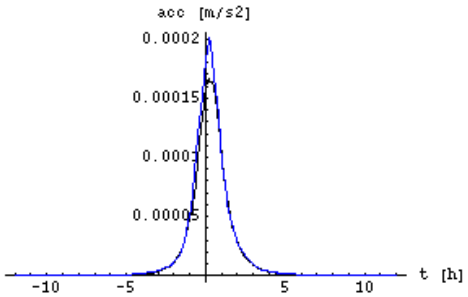

Figure 13. Corrected dust local density scaling

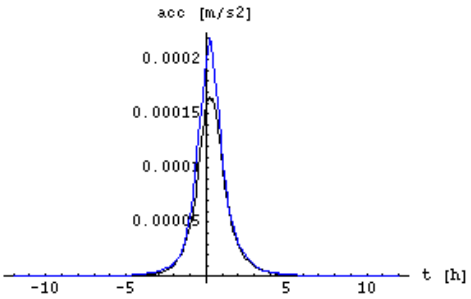

Figure 14. CA-density scaling

7.2.2 Predictions of case 3 from case 2

Fly-by cases 2 and 3 have the same closest-approach distance but fly over a different path on the nucleus surface. Because of that, the R-squared method, which is a good starting point between cases with the same η, yields in this case a very bad prediction, with an error near 70%.

A bit better, but still poor, are the results of the CA-density scaling. Although the method incorporates the actual value of the density at the CA position of both fly-bys, the density profile encountered by the SC during the fly-by is very different for both cases. Consequently, prediction errors are over 43%. Note from Fig. 20 how, although the error in the prediction of the maximum acceleration is quite small, the whole prediction curve is shifted, which results in a large overall error. Indeed, a similar shift will be present in the prediction of all methods but those based on a LS fit, provided that the value of η differs significantly between both fly-bys.

The gas-column-density-scaling represents in this case an improvement with respect to the simple R-squared scaling, because the change in fly-by geometry is partially accounted for with the factor I_p^c / I_m^c. Overall error is reduced below 40%.

The dust-column-density-scaling also improves the results of the R-squared scaling, but this time the overall error remains at about 57%. The reason is that, as shown in Fig. 3, the terminal velocity of dust is not uniform over different points of the nucleus surface, and this results in a significant intrinsic error, because η is very different between one fly-by and the other. The predictions from the gas-column-density scaling method are indeed better because the gas velocity is closer to uniform over different points on the nucleus surface.

We can, however, refine these results by incorporating information about these differences on dust velocity. This reduces the error below 34%, prediction error of the corrected-dust-column-density method. We can at this point verify numerically what we already saw from Fig. 4, nominally that the square root of the ratio of gas densities at a given distance (5 km in this case) is a relatively good predictor of the ratio of dust velocities. From Tab. 2, the square root of the ratio of gas densities is 0.664, whereas the ratio of dust velocities is 0.787.

Still more accurate are the predictions from the gas-local-density-scaling. The use of the gas density distribution given by Eq. 46 whose coefficients $\{a_s, b_s, c_s, d_s\}$ were fitted with the LS

method and provided in section 7.2.1, proves very adequate for this case, in which the acceleration during a fly-by is predicted from the acceleration during a significantly different geometrical scenario. Overall error drops to about 25% (Δv is overstated, as we could have anticipated from Fig. 7, for α = –45 degrees). This result can be further refined by incorporating the actual value of gas density at CA positions. This way, the corrected-gas-local-density scaling reduces the error below 17%.

Considerably worse is the prediction of the dust-local-density-scaling, for reasons identical to those that justify the mediocrity of the results attained with dust-column-density-scaling, i.e. the assumption of uniform dust velocity is very unrealistic. As a consequence, prediction error is in the order of 44%.

This prediction is however extraordinarily improved when differences on dust velocities are accounted for. This is what the corrected-dust-local-density-scaling method does, achieving a remarkably low error of around 10% for such a challenging scenario. Nevertheless, a look at Fig. 22 makes it clear that under a different scenario the method would not have yield so accurate integral results. Acceleration is overstated by more than 10% at its peak, just that this higher Δv is partially compensated by an underestimation thereafter.

Table 6. Estimations for case 3 from case 2

Method	Δv [m/s]	Error Δv (%)	Method	Δv [m/s]	Error Δv (%)
Actual values	0.71930	-	R-squared scaling	1.1117	68.01%
CA-density scaling	0.48959	43.06%	Gas column density scaling	0.82568	39.13%
Dust column density scaling	1.0161	56.96%	Corrected dust column density scaling	0.67553	33.85%
Gas local density scaling	0.90270	25.40%	Corrected gas local density scaling	0.61221	16.62%
Dust local density scaling	1.0356	44.12%	Corrected dust local density scaling	0.68772	10.50%

Actual (black) vs predicted acceleration (blue) for case 3 from data for case 2

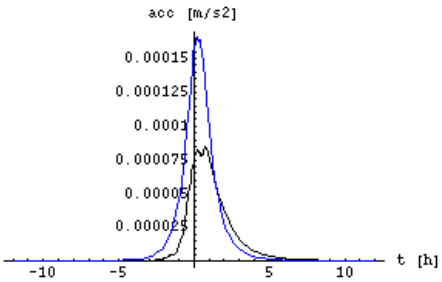

Figure 15. R-squared scaling

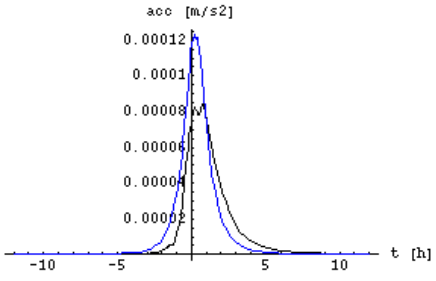

Figure 16. Gas column density scaling

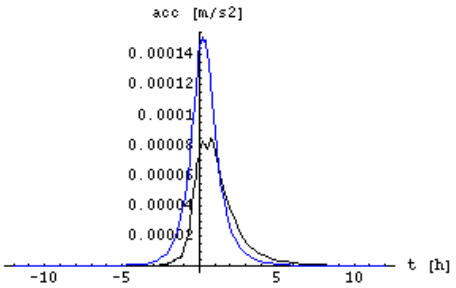

Figure 17. Dust column density scaling

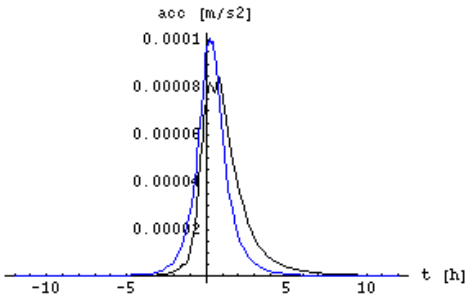

Figure 18. Corrected dust column density scaling

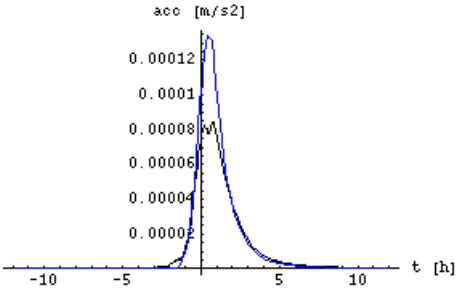

Figure 19. Gas local density scaling

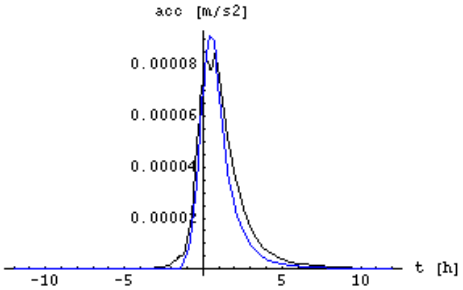

Figure 20. Corrected gas local density scaling

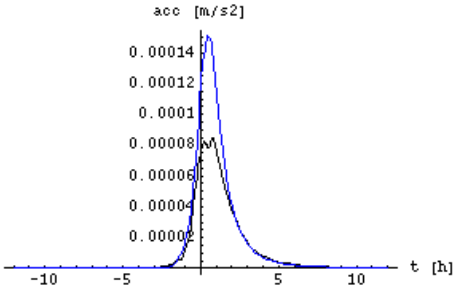

Figure 21. Dust local density scaling

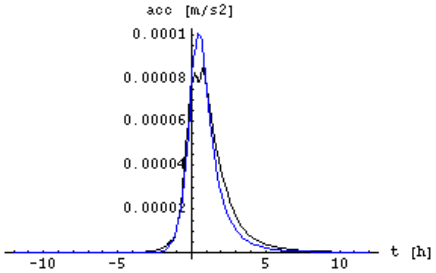

Figure 22. Corrected dust local density scaling

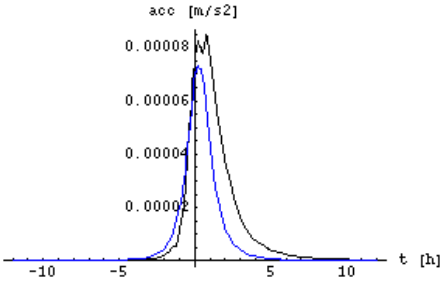

Figure 23. CA-density scaling

7.2.3 Predictions of case 3 from case 1

Finally, we propose the case in which estimations of a fly-by with CA distance of 10 km and $\eta = 0$ (case 1) are used to predict the effect of the coma on the SC for a fly-by with CA distance of 5 km and $\eta = 45$ (case 3). Because both d and η differ significantly between the measured and the predicted fly-bys, this is the most challenging scenario. In fact, the difficulties encountered in the two previous scenarios are compounded.

As expected, the R-squared scaling is too simple for this case (error close to 75%), and both the gas- and dust-column-density-scaling methods achieve modest improvements (errors of about 55% and 60%, respectively). The CA-density-scaling seems more appropriate in this scenario, with an overall error below 38%. After all, the CA-density-scaling method incorporates the actual value of gas density at the CA position of both fly-bys, and this information proves to be more valuable than column-densities for this particular scenario. But again, the prediction from dust column density is drastically improved when predictions on variations on dust velocity are accounted for. This way, the corrected-dust-column-density method reduces the overall error to a meritorious 37%.

Nevertheless, it is the methods that make use of the LS fits of gas and dust density that, once again, yield the best outcomes. While the gas-local-density scaling provides an estimation with overall error below 27%, the corrected-gas-local-density scaling reduces this error to about 9%. Similarly, while the dust-local-density scaling yields an error of about 46%, the prediction error drops to about 13% when estimations of dust velocity are incorporated in the corrected-dust-local-density scaling.

Table 7. Estimations for case 3 from case 1

Method	Δv [m/s]	Error Δv (%)	Method	Δv [m/s]	Error Δv (%)
Actual values	0.72576	-	R-squared scaling	1.1450	74.10%
CA-density scaling	0.60427	37.59%	Gas column density scaling	0.97951	55.27%
Dust column density scaling	1.0280	60.48%	Corrected dust column density scaling	0.68259	37.51%
Gas local density scaling	0.90325	26.48%	Corrected gas local density scaling	0.73635	9.28%
Dust local density scaling	1.0403	45.75%	Corrected dust local density scaling	0.75633	13.19%

Actual (black) vs predicted acceleration (blue) for case 3 from data for case 1

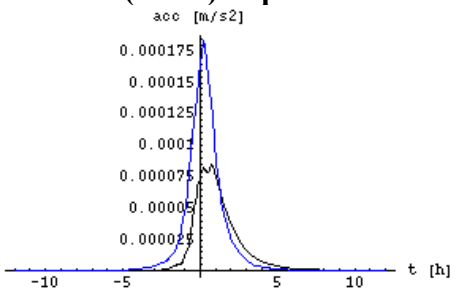

Figure 24. R-squared scaling

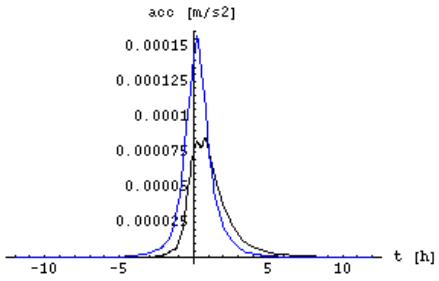

Figure 25. Gas column density scaling

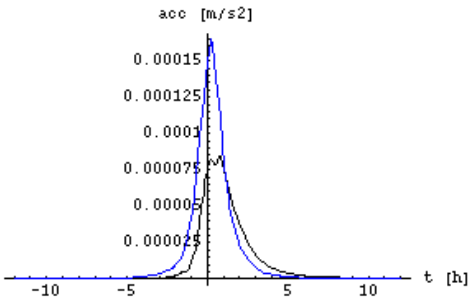

Figure 26. Dust column density scaling

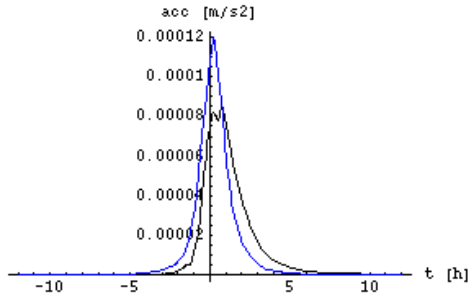

Figure 27. Corrected dust column density scaling

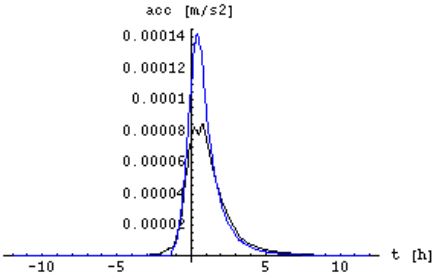

Figure 28. Gas local density scaling

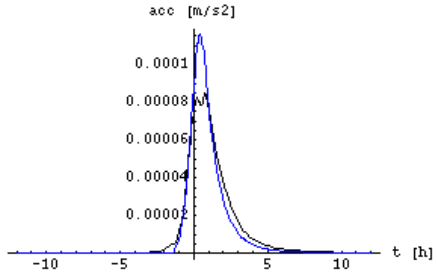

Figure 29. Corrected gas local density scaling

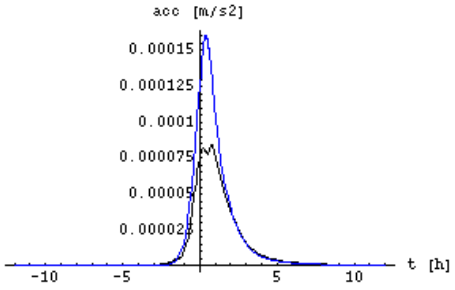

Figure 30. Dust local density scaling

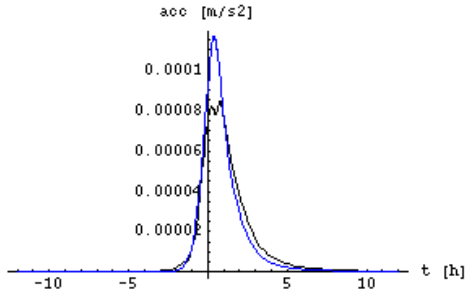

Figure 31. Corrected dust local density scaling

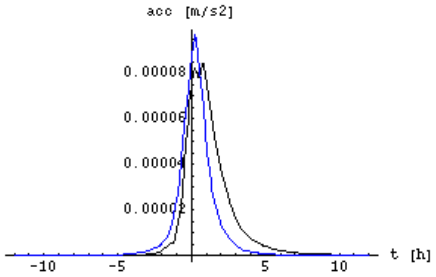

Figure 32. CA-density scaling

8. Conclusions

From the results of the simulation exercise, it is apparent that whenever the coma state changes significantly from one fly-by to the next or the effect of the coma drag on the SC needs to be predicted from data collected during previus fly-bys with significantly different geometries, measurements from remote-sensing instruments need to be incorporated into the scaling process.

For the fly-by cases of our study, both gas images taken from adequate points of view, and the combination of dust images taken from adequate points of view plus estimations of the gas density at CA, make it feasible to predict the dV due to drag with overall errors below 30%. On the other hand, if only estimations of the gas density at CA are available, prediction errors are in the order of 50%. For any scenario, best methods yield an accuracy of 10 - 20% of the dV due to drag. All these figures are under the assumption of availability of error-free measurements of the observables.

Prediction errors are attributed to the fact that the available observables cannot separate relevant physical processes realiably (e.g. the increasing gas velocity with distance from the nucleus). The availability of reliable predictions of the drag force will ultimately depend on the fulfillment of the idealistic assumptions on which the prediction methods are based, principally steady-state coma, no gas compostion or dust-to-gas ratio variation, and constant nucleus surface temperature. However, it will not be until Rosetta reaches the vicinities of the comet that its actual behaviour will be known.

9. References

[1] Probstein, “The Dusty Gasdynamics of Comet Heads” in Problems of Hydrodynamics and Continuum Mechanics SIAM, 568-583, 1968.

[2] Gulkis et al. “Miro: Microwave Instrument for Rosetta Orbiter”, Space Science Reviews 128: 561-597, 2007.